

Opposite phase changes of precipitation annual cycle over land and ocean under global warming

Fengfei Song¹, Jian Lu², Ruby Leung³, and Fukai Liu⁴

¹Pacific Northwest National Laboratory

²Pacific Northwest National Laboratory (DOE)

³PNNL

⁴Ocean University of Qingdao

November 23, 2022

Abstract

The annual cycle of precipitation is a fundamental aspect of the global water cycle. Climate warming induces amplitude enhancement and phase delay in the zonal-mean tropical precipitation. Here, we report a land-ocean contrast in the phase response of precipitation annual cycle, with a delay over land and an advance over ocean as climate warms. Although two-thirds of the Earth's surface are covered by ocean, land dominates the zonal-mean phase delay, attributable to an increase in the effective atmospheric heat capacity. The phase advance over ocean is associated with a precipitation shift from land to ocean during the peak rainy season. This shift is well constrained by the energetic and related to a land-ocean contrast in the amplitude change of surface temperature annual cycle: seasonally different wind changes enhance this amplitude over ocean, while increased effective atmospheric heat capacity and surface cooling feedback reduce the amplitude over land.

1 **Opposite phase changes of precipitation annual cycle over land and**
2 **ocean under global warming**

3 Fengfei Song¹, Jian Lu^{*1}, L. Ruby Leung^{*1}, Fukai Liu²

4 1. Atmospheric Sciences and Global Change Division, Pacific Northwest National Laboratory,
5 Richland, Washington, USA

6 2. Physical Oceanography Laboratory/CIMST, Ocean University of China and Qingdao National
7 Laboratory for Marine Science and Technology, Qingdao, China

8

9 * Corresponding authors: Jian Lu and L. Ruby Leung

10 Email: jian.lu@pnnl.gov and ruby.leung@pnnl.gov

11

12 Fengfei Song: (Orcid-ID: 0000-0002-3004-1749)

13 L. Ruby Leung: (Orcid-ID: 0000-0002-3221-9467)

14 Jian Lu: (Orcid-ID: 0000-0001-8245-6930)

15 Fukai Liu: (Orcid-ID: 0000-0002-0687-9568)

16

17 Submitted to *Geophysical Research Letters*

18 **Keypoints:**

19 1. Precipitation annual cycle shows a phase delay over land but a phase advance over ocean under
20 global warming;

21 2. The land delay is due to enhanced effective atmospheric heat capacity and the ocean advance is
22 linked to land-ocean rainfall shift in summer;

23 3. The enhanced and reduced surface temperature annual cycle over ocean versus land contribute
24 to the rainfall shift via energetic constraint.

25 **Abstract**

26 The annual cycle of precipitation is a fundamental aspect of the global water cycle. Climate
27 warming induces amplitude enhancement and phase delay in the zonal-mean tropical precipitation.
28 Here, we report a land-ocean contrast in the phase response of precipitation annual cycle, with a
29 delay over land and an advance over ocean as climate warms. Although two-thirds of the Earth's
30 surface are covered by ocean, land dominates the zonal-mean phase delay, attributable to an
31 increase in the effective atmospheric heat capacity. The phase advance over ocean is associated
32 with a precipitation shift from land to ocean during the peak rainy season. This shift is well
33 constrained by the energetic and related to a land-ocean contrast in the amplitude change of surface
34 temperature annual cycle: seasonally different wind changes enhance this amplitude over ocean,
35 while increased effective atmospheric heat capacity and surface cooling feedback reduce the
36 amplitude over land.

37 **Plain language summary**

38 The seasonal monsoon rainfall provides the water resource for ~40% of the world population, but
39 it has been a longstanding challenge to predict when monsoon rain will arrive, especially at the
40 regional scale. By separating land from ocean, we revealed that the previous finding of seasonal
41 delay of zonal-mean rainfall under warming mainly occurs over land, where most human activities
42 take place, while ocean shows a phase advance. This contrasting phase behavior between land and
43 ocean is shown to be rooted in the first-principle physical constraints related to energy and climate
44 feedbacks, thus confidence is assigned to the differential phase response between the tropical land
45 and ocean under climate warmng.

46 **1. Introduction**

47 Over the annual cycle, the most prominent hydrological feature is the advance and retreat
48 of tropical rainfall following the movement of monsoons and inter-tropical convergence zone
49 (ITCZ). The annual cycle of tropical rainfall is ultimately driven by solar insolation, but its exact
50 evolution is determined by a myriad of factors, including land-ocean distribution, land surface
51 properties and ocean heat fluxes. Global warming is poised to substantially delay the cyclic
52 progression of tropical rainfall, especially over the monsoonal regions (Biasutti and Sobel 2009;
53 Seth et al. 2011 2013; Pascale et al. 2016; Song et al. 2018a) and enhance its amplitude (Chou et
54 al. 2011; Chou and Lan 2012; Huang et al. 2013). The enhanced tropical precipitation annual cycle
55 mainly occurs over ocean and is due to the increase of moisture under global warming as a “wet-
56 get-wetter” response (Held and Soden 2006; Chou et al. 2009). The seasonal delay of tropical
57 rainfall will induce seasonally-dependent subtropical high responses under warming (Song et al.
58 2018a, b).

59 In the past decade, the atmospheric energetic framework (e.g., Kang et al. 2008; Frierson
60 et al. 2013; Schneider et al. 2014; Boos and Korty 2016; Biasutti et al. 2018) has been developed
61 to relate the ITCZ shift to changes in the net energy input and/or the effective atmospheric heat
62 capacity (Song et al. 2018). The causes of the delay are only beginning to be unveiled through the
63 lens of this energetic perspective (Biasutti and Sobel 2009; Song et al. 2018a). Both the seasonal
64 delay of sea surface temperature (SST) and the annual-mean SST warming can lead to a seasonal
65 delay of tropical precipitation (Biasutti and Sobel 2009; Song et al. 2018; Dwyer et al. 2014). The
66 former is attributed to the high-latitude sea ice melting, which boosts the effective heat capacity of
67 the system by exposing the thick ocean mixed layer to the atmosphere (Dwyer et al. 2012; Donohoe
68 and Battisti 2013). The latter can be explained by the increase of the effective atmospheric heat

69 capacity mainly due to the increase in atmospheric moisture with warming, resulting in a more
70 sluggish response of atmospheric heat transport (AHT) and precipitation to the seasonal solar
71 forcing (Song et al. 2018a; Cronin and Emanuel 2013).

72 Mechanisms that have been used to explain the phase change in the annual cycle of
73 precipitation do not distinguish between the response over land and ocean. As land and ocean
74 differ in many ways, differentiating their phase responses is a natural next step towards
75 understanding regional water cycle in a warming climate. In this study, we find that under global
76 warming, the phase of tropical precipitation is delayed over land but advanced over ocean.
77 Interestingly, despite covering only one-third of the Earth's surface, it is land, not ocean, that
78 dominates the phase changes of zonal-mean precipitation annual cycle. The opposite phase
79 changes between land and ocean will have profound implications for both terrestrial/marine
80 ecosystems and human activities.

81

82 **2. Data and methods**

83 **2.1 Model simulation data**

84 Monthly mean data of multiple variables from 37 Coupled Model Intercomparison Project
85 Phase 5 (CMIP5; Taylor et al. 2012) models and daily precipitation data from 40 members of
86 CESM1 Large Ensemble (LENS) Project (Kay et al. 2015) are used in this study. The statistics of
87 the present-day climate for 1962-2005 are from the historical (HIST) simulations while those for
88 the future climate of 2056-2099 are from the RCP8.5 (RCP85) scenario simulations.

89 To examine the role of wind-evaporation-SST (WES) feedback on the phase changes of
90 precipitation annual cycle, we also analyze two sets of experiments: one with the same fully

91 coupled CESM1 as used for the CESM LENS Project and the other with a partially coupled
 92 configuration of CESM1 (Liu et al. 2018). Each set consists of a pair of 100-year long simulations
 93 with one under the condition of pre-industrial CO₂ (1xCO₂) and the other with CO₂ quadrupling
 94 (4xCO₂). In the partially coupled set, the wind speed from the pre-industrial simulation is prescribed
 95 through the bulk formula that is used to compute the evaporation over ocean in both the 1xCO₂
 96 and 4xCO₂ runs, so that the part of the climate change response due to WES feedback is disabled.
 97 Comparing the response to 4xCO₂ forcing between the fully coupled and partially coupled sets
 98 allows the role of the WES feedback to be isolated. See Liu et al. (2018) for more details about the
 99 design of the experiments.

100 **2.2 Phase estimated from the first Fourier harmonic**

101 To estimate the phase of the annual cycle, Fourier transformation is performed to fit the
 102 related monthly time series to a Fourier harmonic (i.e., a sinusoidal function with time) with an
 103 angular frequency of $2\pi/12\text{mon}$. As the first Fourier harmonic explains more than 90% of
 104 variance in most models, we only use it to determine the phase of the annual cycle.

105 **2.3 Atmospheric energetic framework**

106 According to the atmospheric energy equation (Neelin and Held 1987), the divergence of
 107 AHT ($\nabla \cdot AHT$) is equal to the difference between the net energy input to the atmosphere F_{net} and
 108 the column moist static energy (MSE) tendency $\frac{\partial \langle h \rangle}{\partial t}$:

$$109 \quad \nabla \cdot AHT = F_{net} - \frac{\partial \langle h \rangle}{\partial t}, \quad (1)$$

110 where the angle bracket represents vertical integration between the surface and the top of the
 111 model, F_{net} includes sensible heat flux, latent heat flux, net longwave radiation and net shortwave
 112 radiation, h is the MSE. Following Boos and Korty (2016), we also isolate the divergent

113 component of the energy flux by solving the inverse Laplacian of energy flux potential χ , which
114 is defined as

$$115 \quad \nabla^2 \chi = \nabla \cdot AHT \quad (2)$$

116

117 **3. Results**

118 Figure 1 shows the future change in the annual cycle of tropical precipitation over land and
119 ocean in both hemispheres. Climatologically, when the peak solar forcing moves across the equator
120 from one hemisphere to another, tropical precipitation increases rapidly in the warmed hemisphere,
121 but the timing of precipitation peak differs between land and ocean, with the former leading the
122 latter by about a month due to its lower heat capacity (solid lines in Fig. 1a-d). Under global
123 warming, there is an intriguing contrast in the future changes between land and ocean (bars in Fig.
124 1a-d): over land, precipitation anomalies peak much later than the climatological peak, while the
125 opposite is true over ocean, indicating a phase delay in the precipitation annual cycle over land but
126 a phase advance over ocean. The larger amplitude changes during the transition seasons over land
127 than ocean accentuate the dominance of the land response in the zonal-mean response.

128 The phase changes over land versus ocean (0-40°N/S) are further quantified. Most CMIP5
129 models (Fig. 1e) and all LENS members (Fig. 1f) exhibit a seasonal delay over land, with median
130 values of 2 to 4.5 days, and a seasonal advance over ocean, with a similar range of median values.
131 For the Northern Hemispheric (NH) land and ocean, 34 and 33 out of 37 CMIP5 models show the
132 phase delay and advance, respectively. Similarly for the Southern Hemispheric (SH) land and
133 ocean, 36 and 29 out of 37 CMIP5 models show the phase delay and advance, respectively.

134 To decipher the contrasting precipitation phase changes between land and ocean, we
135 conduct Empirical Orthogonal Function (EOF) analysis on the annual cycle of precipitation and
136 identify two dominant modes (Fig. 2; Wang and Ding 2008): one characterized by an inter-
137 hemispheric contrast (EOF1; accounting for 67.9% of variance) with a peak during local summer
138 and the other featuring a distinct land-sea contrast (EOF2; accounting for 18.6% of variance) with
139 a peak during local spring. Precipitation center tends to be well collocated with the local maxima
140 of column MSE (contours in Figs. 2a-b). The phase change in both PCs is in quadrature to the
141 phase of the corresponding climatological PCs, indicating a phase delay (Fig. 2c-d). The phase
142 delay in the EOF1 has been attributed to both the phase delay in the annual cycle of SST and the
143 annual-mean SST warming as explained above. The similar phase delays in PC1 and PC2 are
144 mainly the result of EOF analysis that requires the EOF modes to be orthogonal to each other. The
145 seasonal delay in both PC1 and PC2 is quite robust among the CMIP5 models and LENS
146 simulations (Fig. 2e), with 36 out of 37 CMIP5 models and 39 out of 40 LENS members showing
147 a delay. Another robust aspect in the response of the two EOF modes under warming is the
148 enhancement of the amplitude in all CMIP5 models and LENS members, with a median increase
149 of ~10% (Fig. 2f), consistent with the enhanced annual cycle of the global monsoon rainfall (Kitoh
150 et al. 2013; Lee and Wang 2014).

151 Were the spatial pattern of the leading two EOF modes unchanged, the delay in their phases
152 would imply a phase delay in the precipitation annual cycle over both land and ocean. But it turns
153 out not to be the case (Fig. 1). As the two leading EOF modes of precipitation annual cycle explain
154 more than 85% of the total seasonal variance, we construct the precipitation annual cycle over land
155 and ocean (P_L and P_O , respectively) based on the two modes as follows:

$$156 \quad P_L = A_{1,L}PC1 + A_{2,L}PC2 \quad (3)$$

157 $P_O = A_{1,O}PC1 + A_{2,O}PC2$ (4)

158 Here, $PC1$ and $PC2$ are the corresponding normalized principle components, $A_{1,L}$ and $A_{2,L}$ are the
 159 amplitudes of EOF1 and EOF2 averaged over land, respectively; $A_{1,O}$ and $A_{2,O}$ are the same but
 160 over ocean.

161 Given the orthogonality of PCs, we can express the $PC1$ and $PC2$ as two sinusoidal
 162 functions with $PC2$ leading $PC1$ by $\pi/2$. Then, the annual cycle of P_L and P_O can be written as:

163 $P_L = \sqrt{A_{1,L}^2 + A_{2,L}^2} \sin(t - \phi_1 - \phi_L)$ (5)

164 $P_O = \sqrt{A_{1,O}^2 + A_{2,O}^2} \sin(t - \phi_1 - \phi_O),$ (6)

165 Here, t is time, ϕ_1 denotes the phase of PC1. It is found that the reconstructed precipitation annual
 166 cycle and the actual one is almost identical. This way, the phases of P_L and P_O are $\phi_1 + \phi_L$ and

167 $\phi_1 + \phi_O$, respectively. $\phi_L = -\arcsin\left(\frac{1}{\sqrt{\left(\frac{A_{1,L}}{A_{2,L}}\right)^2 + 1}}\right)$ and $\phi_O = \arcsin\left(\frac{1}{\sqrt{\left(\frac{A_{1,O}}{A_{2,O}}\right)^2 + 1}}\right)$ represent extra

168 phase associated with the relative contribution of EOF1 versus EOF2 to the land and ocean annual
 169 cycle, respectively. Under warming, if the amplitude of EOF1 increases more than EOF2 over

170 land, $\frac{A_{1,L}}{A_{2,L}}$ becomes larger and the resultant change in ϕ_L would imply a delay. The opposite is true

171 over ocean (note the opposite signs between ϕ_L and ϕ_O). The actual land-ocean phase change
 172 differences (Fig. 1e-f) can be well explained by their amplitude-based estimates (i.e., $\phi_L - \phi_O$),

173 with correlation of 0.97 and 0.89 in NH and SH, respectively (Supplementary Fig. 1), lending

174 support to the decomposition framework here. Hence, the land-sea difference in phase changes of

175 precipitation annual cycles can also be casted in terms of the spatial pattern changes in EOF1 and
176 EOF2 (i.e., $\frac{A_{1,L}}{A_{2,L}}$ and $\frac{A_{1,O}}{A_{2,O}}$).

177 Figure 3a shows a weak reduction in $\frac{A_{1,L}}{A_{2,L}}$, but a marked increase in $\frac{A_{1,O}}{A_{2,O}}$ in both hemispheres
178 ($\frac{A_{1,O}}{A_{2,O}}$ increases by 38% and 29% for NH and SH, respectively) under warming, with the former
179 opposing slightly the delay in ϕ_1 by an amount ϕ_L , while the latter overwhelming the positive
180 change in ϕ_1 , resulting in a net phase advance in P_O (i.e., $\phi_O + \phi_1 < 0$) shown in Fig. 1. Further
181 examination indicates that the increase in $\frac{A_{1,O}}{A_{2,O}}$ is dominated by the increase in $A_{1,O}$ (Fig. 3b), with
182 $A_{2,O}$ showing negligible changes (not shown). The change of EOF1 precipitation pattern (Fig. 3c)
183 features large increases over broad tropical oceans, while the change is only marginal over tropical
184 land, indicating a shift of precipitation from land to ocean during local summer when EOF1 peaks.
185 This shift is robust in terms of the land-minus-ocean precipitation change among CMIP5 models
186 (Supplementary Fig. 2a).

187 What tilts the land-ocean precipitation balance towards ocean in EOF1? As the “wet-get-
188 wetter” response doesn’t hold well over land due to the limited moisture supply (Fasullo 2012;
189 Chadwick et al. 2013; Byrne and O’Gorman 2015; Donat et al. 2016), it may not be surprising that
190 the land precipitation change is subdued relative to the ocean response. Here we explore other
191 possible mechanisms via the energetic perspective. Viewing from the energetic constraint on
192 precipitation, the land-ocean precipitation shift in EOF1 should be associated with an AHT from
193 ocean to land, and indeed this is evidenced by the direct calculation of the change in AHT
194 divergence contrast between land and ocean (Fig. 3c; Supplementary Fig. 2). This divergent flow
195 of MSE appears to be from the warmer ocean to the colder land (Fig. 3c&d). According to the
196 convective quasi-equilibrium argument suitable for the tropical convective regions (Emanuel

197 1995; Shekar and Boos 2016), the column MSE is approximately in equilibrium with the sub-
198 cloud entropy, which is in turn regulated by the surface temperature (TS) when the surface relative
199 humidity is high. With the diffusive nature of energy transport (Boos and Korty 2016), AHT should
200 point from higher MSE to lower MSE regions and hence from the relatively warmer TS to the
201 colder TS regions. The correlation between the land-sea contrast of AHT divergence and TS
202 changes among CMIP5 models is 0.81 and 0.63 in NH and SH, respectively. Even over land, the
203 corresponding correlation is 0.70 and 0.54, still statistically significant at 1% level. Previous
204 studies (e.g., Hurley and Boos 2013; Roderick et al. 2014) suggested that over land, TS is mainly
205 driven by precipitation when evaporation is limited. If so, the TS change would be negatively
206 correlated with the change in precipitation and AHT divergence. Here, the significantly positive
207 correlation between TS and AHT divergence changes over land implies the decreased TS over
208 land does play a role in the suppressed precipitation in summer. As such, the land-sea precipitation
209 shift during summer is linked to the opposite amplitude changes in the TS annual cycle over land
210 and ocean, which is the focus of our investigation next.

211 Over ocean, a robust climate change response is the strengthening of surface wind in the
212 winter subtropics and the weakening in the summer subtropics (Sobel and Camargo; contours in
213 Fig. 3d). As wind speed is identified to be important in the tropical SST warming pattern formation
214 (Xie et al. 2010), the contrasting wind response induces relative cooling in the winter subtropics
215 and warming in the summer subtropics via WES feedback (Xie and Philander 1994; Lu and Zhao
216 2012), leading to the enhanced SST annual cycle (Fig. 3d). Thus, more rainfall occurs over ocean
217 during summer, resulting in a phase advance over ocean. To further support our hypothesis, the
218 CESM1 experiments with active WES reproduce the opposite phase changes of precipitation
219 annual cycle over land and ocean (red crosses in Fig. 1f). When the WES feedback is disabled in

220 the 4xCO₂ experiments, the phase advance over ocean is completely nullified in NH and reduced
221 by more than half in SH, whereas the land phase delay mostly persists (blue crosses in Fig. 1f).

222 In contrast to the increased amplitude of TS over ocean, the amplitude of TS is reduced
223 over land, most notably in the monsoon regions (Fig. 3d). The governing mechanism for the annual
224 cycle of temperature over land can be captured by an atmosphere-land surface interaction model
225 forced by a periodic solar insolation:

$$226 \quad C_A \frac{dT_A}{dt} = \lambda(T_S - T_A) - B T_A \quad (7)$$

$$227 \quad C_S \frac{dT_S}{dt} = -\lambda(T_S - T_A) + R, \quad (8)$$

228 where T_A is the mass-weighted temperature of the column atmosphere, which is dominated by the
229 near surface air temperature, T_S is the land TS, C_A and C_S are the effective heat capacities of the
230 atmosphere and surface, respectively. The total surface-atmosphere energy exchange including
231 longwave radiation, sensible and latent heat fluxes is parameterized to be linearly proportional to
232 $T_S - T_A$ with an exchange coefficient λ (as similarly treated in Barsugli and Battisti (1998) and
233 Zhou and Xie (2018)). B is the bulk feedback parameter accounting for all the radiative processes
234 at the top of atmosphere, including water vapor, cloud, lapse rate and Planck feedbacks. Since the
235 adjustment of T_A through the top of the atmosphere is slower than that at the surface, B is generally
236 smaller than λ (Barsugli and Battisti 1998). The system is forced at the surface by a periodic solar
237 radiation R with a frequency of yr⁻¹, hence shortwave absorption by the atmosphere is neglected.

238 Over tropical land, C_S is estimated to be one order smaller than C_A . Thus, adding Eqs. (7)
239 and (8) together and ignoring the small term associated with C_S reduce the system to a single
240 variable system:

241 $C_A \frac{dT_A}{dt} = -BT_A + R,$ (9)

242 from which the amplitude relation between T_A and R can be derived:

243 $|T_A| = \frac{|R|}{\sqrt{B^2 + \omega^2 C_A^2}},$ (10)

244 where $\omega = 2\pi yr^{-1}$. Under the condition $\omega C_A \ll \lambda$, which holds well for the modern climate
 245 condition, the amplitude relation between T_A and T_S can be written as:

246 $|T_S| \approx (1 + \frac{B}{\lambda})|T_A|,$ (11)

247 Thus, for a given solar insolation, the amplitude of atmospheric temperature decreases with the
 248 increase in the effective atmospheric heat capacity and bulk feedback parameter B . The same may
 249 also be said of the amplitude of T_S considering the linear relationship between T_S and T_A from Eq.
 250 (11).

251 Following Schwartz (2007), the effective atmospheric heat capacity is defined as $C_A =$
 252 $\frac{\partial \langle h \rangle / \partial t}{\partial \langle T \rangle / \partial t}$, with $\langle h \rangle$ and $\langle T \rangle$ representing the vertically-integrated MSE and temperature. This
 253 definition of C_A allows to estimate it by regressing the monthly tendency of multi-model ensemble
 254 mean $\langle h \rangle$ against that of $\langle T \rangle$. Based on this definition, C_A can be scaled as $C_A \approx c_p + \frac{L_v \langle q \rangle}{\langle T \rangle}$,
 255 where $\langle q \rangle$ is the vertically integrated water vapor. As $\langle q \rangle$ increases nonlinearly with
 256 temperature following the Clausius-Clapeyron relation, C_A increases as the mean climate warms.
 257 Song et al. (2018a) has already shown that the annual cycle of $\partial \langle h \rangle / \partial t$ is robustly enhanced
 258 mainly due to the contribution from $\partial \langle L_v q \rangle / \partial t$, which scales linearly with global warming.
 259 Here, we provide further evidences for the increase of effective atmospheric heat capacity
 260 (Supplementary Fig. 3). In the current climate, C_A is 2162.10 and 2704.01 J kg⁻¹ K⁻¹ for NH and

261 SH, respectively. Under global warming, C_A is increased to 2393.10 and 3271.39 J kg⁻¹ K⁻¹, with
 262 an increase rate of 10.7% and 21.0% for NH and SH, respectively. The enhancement of C_A is
 263 ubiquitous across all CMIP5 models examined (Supplementary Fig. 4). As no robust change in B
 264 is found over tropical land under warming in CMIP5 models, the robust increase of the effective
 265 atmospheric heat capacity acts to reduce the amplitude of the T_A and T_S annual cycle over land,
 266 consistent with Cronin and Emanuel (2013) based on radiative-convective equilibrium
 267 simulations.

268 Since a good proportionality holds between T_A and T_S with small phase differences for the
 269 system above, we can further simplify Eq. (8) into a surface energy balance model for T_S :

$$270 \quad C_S \frac{dT_S}{dt} = -\beta T_S + R, \quad (12)$$

271 where β is a parameter to measure the surface cooling feedback, encompassing processes of net
 272 longwave radiative cooling and turbulent heat fluxes. A similar surface energy model has been
 273 used to understand the temperature annual cycle in an extraterrestrial planet (Mitchell et al. 2014),
 274 where only longwave radiation is considered in the damping term. The amplitude of T_S governed
 275 by Eq. (12) is determined by

$$276 \quad |T_S| = \frac{|R|}{\sqrt{\beta^2 + \omega^2 C_S^2}}, \quad (13)$$

277 and is expected to decrease with an increase of the feedback parameter β . We estimate β by
 278 regressing the total surface energy flux excluding the shortwave fluxes on the annual cycle of TS
 279 for both current and future climates. The resultant β is generally positive over land in the current
 280 climate (Supplementary Fig. 5a), vindicating its physical meaning as a damping parameter. In the
 281 tropical monsoonal regions, β indeed increases across the majority of CMIP5 models under the

282 RCP85 scenario and geographically, it coincides with regions of decreased TS annual cycle (Fig.
283 3d and Supplementary Fig. 5b). Averaged over the land monsoonal regions, the change of β is
284 significantly (at 1% level) correlated with that of summer-vs-winter TS difference across the
285 CMIP5 models, with correlations reaching -0.68 in NH and -0.46 in SH (or -0.81 with the outlier
286 models excluded) (Supplementary Fig. 6). Taken together, both the increase of C_A and β work in
287 tandem to dampen the TS amplitude over land.

288

289 **4. Conclusions**

290 This study discovers intriguing opposite phase changes in the precipitation annual cycle
291 between land and ocean under climate warming: a delay over land, but an advance over ocean.
292 Although land only covers one-third of the Earth's surface, it dominates the phase delay of zonal-
293 mean precipitation annual cycle previously found (Biasutti and Sobel 2009; Song et al. 2018a).
294 The delay over land is mainly determined by the increased effective atmospheric heat capacity
295 under warming, the same mechanism responsible for the zonal-mean precipitation delay (Song et
296 al. 2018a). The phase advance over ocean is related to a shift of precipitation center towards ocean
297 in the local summer, which overwhelms the phase delay resulting from the increased effective
298 atmospheric heat capacity. The shift of precipitation from land to ocean during the peak rainy
299 season corresponds well to the pattern of AHT divergence change, epitomizing the energetic
300 constraint on the tropical precipitation change even at the regional scale. The AHT divergence
301 change under climate warming is closely related to the opposite changes in the amplitude of TS
302 annual cycle between land and ocean. The strengthened surface wind in winter cools SST and the
303 weakened one in summer warms SST, enhancing the amplitude of SST annual cycle. Over land,
304 on the other hand, both the increased effective atmospheric heat capacity and surface cooling

305 feedback over monsoonal regions act to dampen the amplitude of TS annual cycle. The
306 combination of enhanced TS amplitude over ocean and reduced TS amplitude over land rebalances
307 the atmospheric column energy in favor of ocean precipitation. As a result, the center of
308 precipitation shifts towards ocean, which is further manifested as a differential phase change
309 between land and ocean.

310 Considering the earlier transition from dry to wet seasons over land than ocean in the
311 climatological annual cycle, the phase delay over land and phase advance over ocean under
312 warming will make the two more in sync in a warmer future. The delayed onset of rainfall as well
313 as the dampened annual cycle of temperature over land would have profound economic and
314 societal impacts, especially for regions like Asia, Africa and Latin America, where the local rainfed
315 agriculture and economy are under the sway of monsoonal rain.

316 **Acknowledgement**

317 This research is supported by the U.S. Department of Energy Office of Science Biological and
318 Environmental Research as part of the Regional and Global Modeling and Analysis program area.
319 PNNL is operated for the Department of Energy by Battelle Memorial Institute under contract DE-
320 AC05-76RL01830. We acknowledge the World Climate Research Program's Working Group on
321 Coupled Modeling, which makes CMIP5 data available ([http://www.ipcc-
322 data.org/sim/gcm_monthly/AR5/Reference-Archive.html](http://www.ipcc-
322 data.org/sim/gcm_monthly/AR5/Reference-Archive.html)) and NCAR CESM1 group, which
323 makes the large-ensemble (LENS) experiments available
324 (<http://www.cesm.ucar.edu/projects/community-projects/LENS/>).

325 **References**

326 Barsugli, J. J. and D. S. Battisti (1998), The basic effects of atmosphere-ocean thermal coupling
327 on midlatitude variability. *J. Atmos. Sci.* 55, 477–493.

328 Biasutti, M. and A. H. Sobel (2009), Delayed Sahel rainfall and global seasonal cycle in a warmer
329 climate. *Geophys. Res. Lett.*, 36, L23707.

330 Biasutti, M., A. Voigt, W. R. Boos, P. Braconnot, J. C. Hargreaves, S. P. Harrison, et al (2018),
331 Global energetics and local physics as drivers of past, present and future monsoons. *Nature*
332 *Geoscience* 11(6), 392-400.

333 Boos, W. R. and R. L. Korty (2016), Regional energy budget control of the intertropical
334 convergence zone and application to mid-Holocene rainfall. *Nat. Geosci.* 9, 892–897.

335 Byrne, Michael P. and Paul A. O’Gorman (2015), The Response of Precipitation Minus
336 Evapotranspiration to Climate Warming: Why the “Wet-Get-Wetter, Dry-Get-Drier” Scaling Does
337 Not Hold over Land. *Journal of Climate* 28, 8078-8092.

338 Chadwick, R., I. Boutle, and G. Martin, (2013) Spatial patterns of precipitation change in CMIP5:
339 why the rich do not get richer in the tropics. *J. Clim.* 26, 3803–3822.

340 Chou, C., J.-Y. Tu and P.-H. Tan (2007), Asymmetry of tropical precipitation change under global
341 warming. *Geophys. Res. Lett.* 34, L17708.

342 Chou, C., J. Neelin, C. Chen and J. Tu (2009), Evaluating the ‘rich-get-richer’ mechanism in
343 tropical precipitation change under global warming. *J. Clim.* 22, 1982–2005.

344 Chou, C. and C-W. Lan (2012), Changes in the annual range of precipitation under global warming.
345 *J. Clim.* 25, 222–235.

346 Cronin, T. W. and K. A. Emanuel (2013), The climate time scale in the approach to radiative-
347 convective equilibrium. *J. Adv. Model. Earth Syst.* 5, 843–849 (2013).

348 Donat, M. G., A. L. Lowry, L. V. Alexander, P. A. O'Gorman and N. Maher (2016) More extreme
349 precipitation in the world's dry and wet regions. *Nat. Clim. Change* 6, 508–513.

350 Donohoe, A. and D. S. Battisti (2013), The seasonal cycle of atmospheric heating and temperature.
351 *J. Clim.* 26, 4962–4980.

352 Dwyer, J. G., M. Biasutti and A. H. Sobel (2012), Projected changes in the seasonal cycle of
353 surface temperature. *J. Clim.* 25(18), 6359–6374.

354 Dwyer, J. G., M. Biasutti and A. H. Sobel (2014), The effects of greenhouse gas-induced changes
355 in SST on the annual cycle of zonal mean tropical precipitation. *J. Clim.* 27, 4545–4565.

356 Emanuel, K. A. (1995), On thermally direct circulation in moist atmosphere. *J. Atmos. Sci.* 52,
357 1529–1534.

358 Fasullo, J. (2012), A mechanism for land–ocean contrasts in global monsoon trends in a warming
359 climate. *Clim. Dynam.* 39, 1137–1147.

360 Frierson, D. M. W. et al (2013), Contribution of ocean overturning circulation to tropical rainfall
361 peak in the northern hemisphere. *Nature Geosci.* 6, 940–944.

362 Held, I. M. and B. J. Soden (2006), Robust responses of the hydrological cycle to global warming.
363 *J. Clim.* 19, 5686–5699.

364 Huang, P., S-P. Xie, K. Hu, G. Huang and R. Huang (2013), Patterns of the seasonal response of
365 tropical rainfall to global warming. *Nature Geosci.* 6, 357–361.

366 Hurley, J. V., and W. R. Boos (2013), Interannual variability of monsoon precipitation and
367 subcloud equivalent potential temperature, *J. Climate*, 26, 9507–9527.

368 Kang, S. M., I. M. Held, D. Frierson and M. Zhao (2008), The response of the ITCZ to extratropical
369 thermal forcing: Idealized slab-ocean experiments with a GCM. *J. Clim.* 21(14):3521–3532.

370 Kay, J. E. et al (2015), The Community Earth System Model (CESM) Large Ensemble Project: A
371 Community Resource for Studying Climate Change in the Presence of Internal Climate Variability,
372 *Bull. Am. Meteorol. Soc.* 96, 1333-1349.

373 Kitoh, A. et al (2013), Monsoons in a changing world: a regional perspective in a global context.
374 *J. Geophys. Res.* 118, 3053–3065.

375 Lee, J.-Y. and B. Wang (2014), Future change of global monsoon in the CMIP5. *Clim Dynam* 42,
376 101–119.

377 Liu, W., J. Lu, S. P. Xie and A. Fedorov (2018), Southern Ocean heat uptake, redistribution, and
378 storage in a warming climate: The role of meridional overturning circulation. *J. Clim.* 31, 4727–
379 4743.

380 Lu, J. and B. Zhao (2012), The role of oceanic feedback in the climate response to doubling CO₂.
381 *J. Clim.* 25, 7544–7563.

382 Mitchell, J. L., G. K. Vallis, and S. F. Potter (2014), Effects of the Seasonal Cycle on Superrotation
383 in Planetary Atmospheres, *The Astrophysical Journal* 787(1), 23.

384 Neelin, J. and I. M. Held (1987), Modeling tropical convergence based on the moist static energy
385 budget. *Mon. Wea. Rev.* 115, 3–12.

386 Pascale, S., V. Lucarini, X. Feng, , A. Porporato & S. Hasson (2016), Projected changes of rainfall
387 seasonality and dry spells in a high greenhouse gas emissions scenario. *Clim. Dyn.* 46, 1331–1350.

388 Roderick, M. L., F. Sun, W. H. Lim, and G. D. Farquhar (2014), A general framework for
389 understanding the response of the water cycle to global warming over land and ocean. *Hydrol.*
390 *Earth Syst. Sci.*, 18, 1575–1589.

391 Schneider, T., T. Bischoff and G. H. Haug (2014), Migrations and dynamics of the intertropical
392 convergence zone. *Nature* 513, 45–53.

393 Schwartz, S. E. (2007), Heat capacity, time constant, and sensitivity of Earth's climate system. *J.*
394 *Geophys. Res.* 112, D24S05.

395 Seth, A., S. A. Rauscher, M. Rojas, A. Giannini and S. J. Camargo (2011), Enhanced spring
396 convective barrier for monsoons in a warmer world? *Climatic Change* 104, 403–414.

397 Seth, A. et al. (2013), CMIP5 projected changes in the annual cycle of precipitation in monsoon
398 regions. *J. Clim.* 26, 7328–7351.

399 Shekar, R. and W. R. Boos (2016), Improving energy-based estimate of monsoon location in the
400 presence of proximal desert. *J. Clim.* 29, 4741-4761.

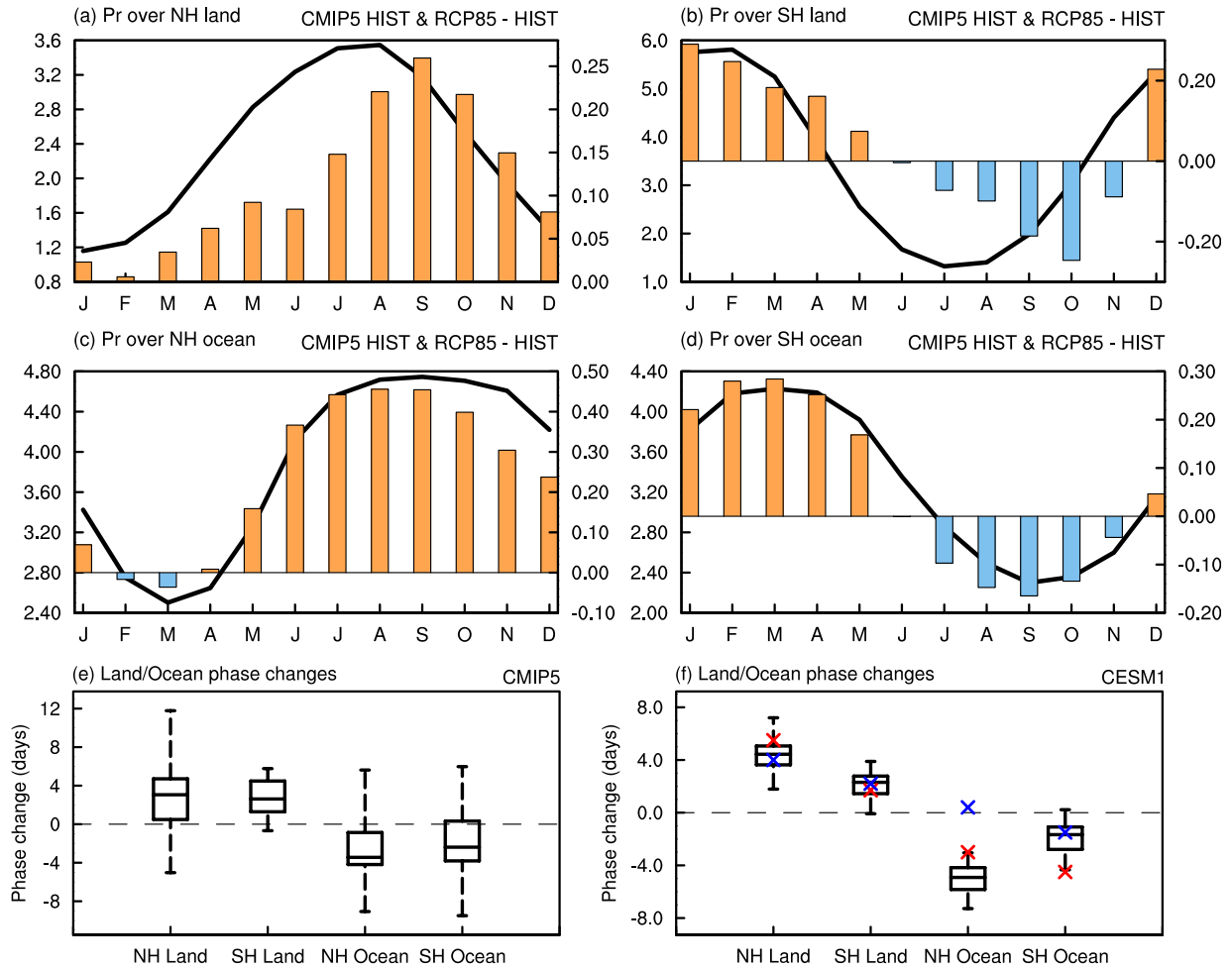
401 Sobel, A. H. and S. J. Camargo (2011), Projected future changes in tropical summer climate. *J.*
402 *Clim.* 24, 473–487.

403 Song, F., L. R. Leung, J. Lu and L. Dong (2018a), Seasonally dependent responses of subtropical
404 highs and tropical rainfall to anthropogenic warming. *Nature Clim. Change* 8, 787–792.

405 Song, F., L.R. Leung, J. Lu and L. Dong (2018b), Future changes in seasonality of the North
406 Pacific and North Atlantic subtropical highs, *Geophysical Research Letters*, 45, 11,959-11,968.

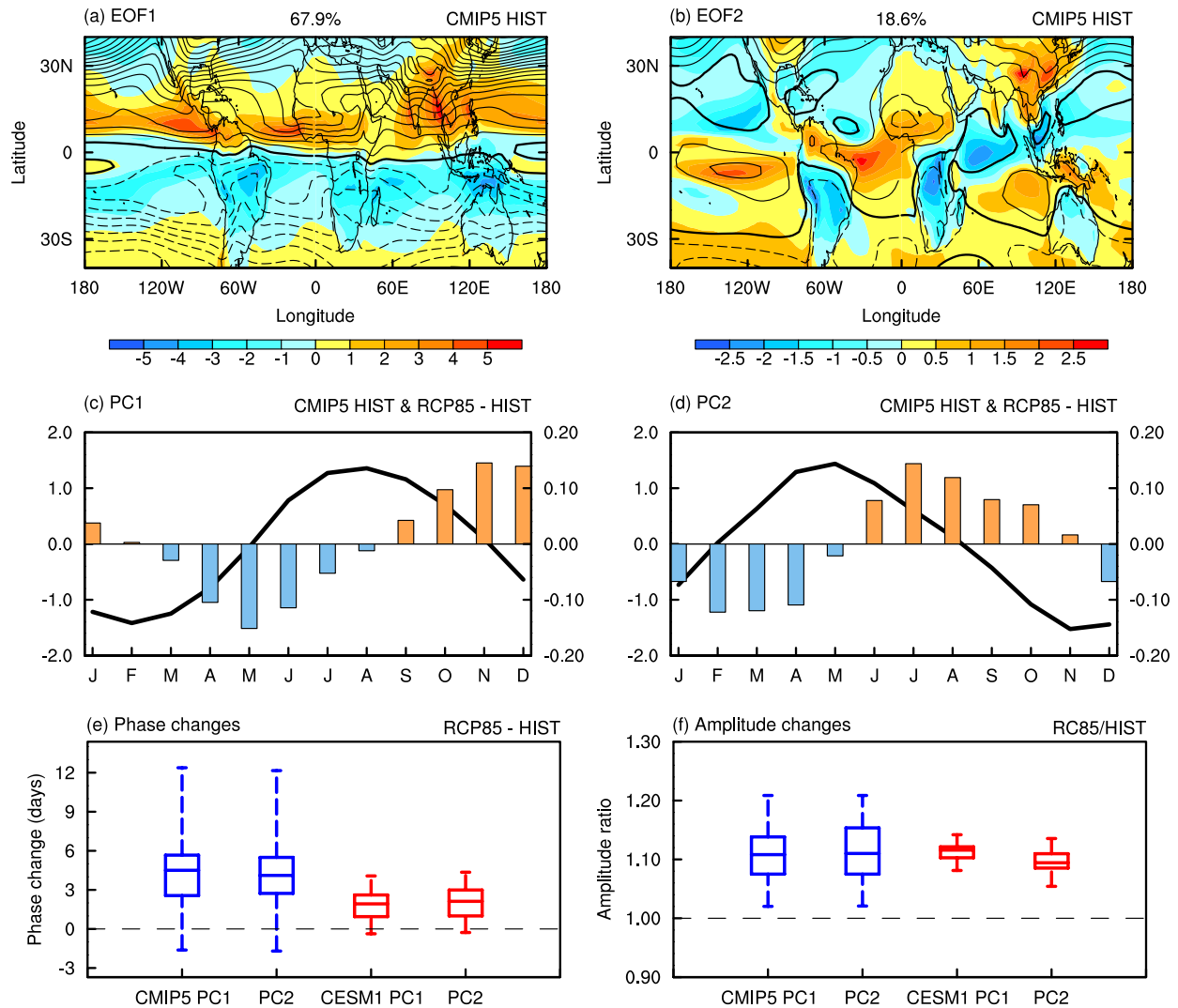
407 Taylor, K. E., R. J. Stouffer, and G. A. Meehl (2012), An overview of CMIP5 and the experiment
408 design. *Bull. Am. Meteorol. Soc.* 93, 485–498.

- 409 Wang, B. and Q. Ding (2008), Global monsoon: Dominant mode of annual variation in the tropics.
410 *Dynam Atmos Oceans* 44, 165–183.
- 411 Xie, S. P. and S. G. H. Philander (1994), A coupled ocean-atmosphere model of relevance to the
412 ITCZ in the eastern Pacific. *Tellus A* 46, 340–350.
- 413 Xie, S. P. et al. (2010), Global warming pattern formation: Sea surface temperature and rainfall. *J.*
414 *Clim.* 23, 966–986.
- 415 Zhou, W., and S. P. Xie (2018), A Hierarchy of Idealized Monsoons in an Intermediate GCM, *J.*
416 *Clim.* 31(22), 9021–9036.



417

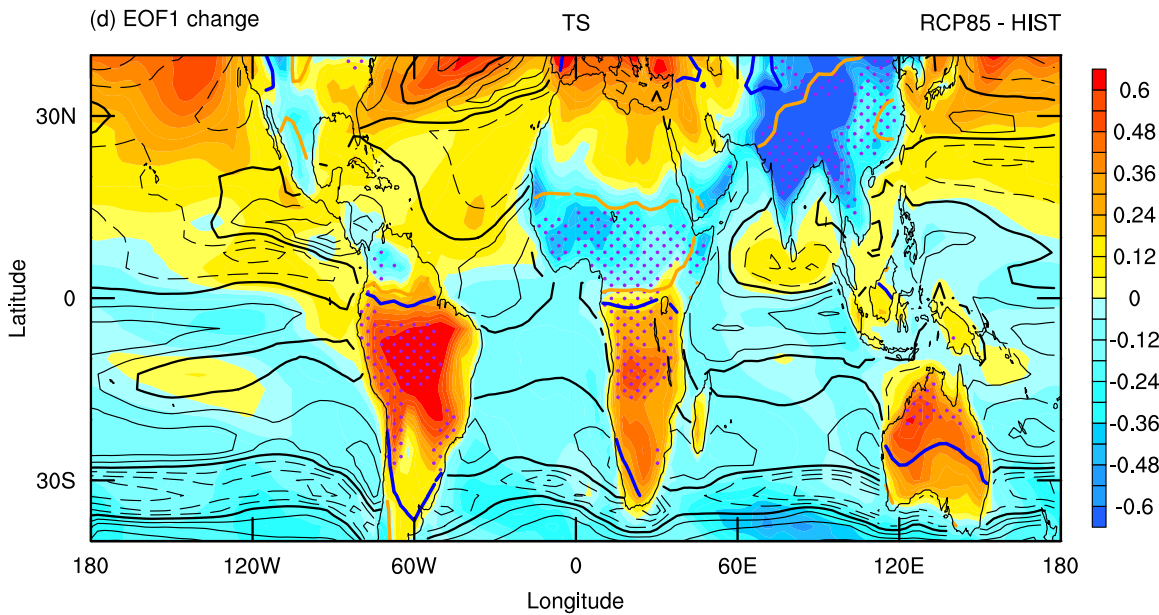
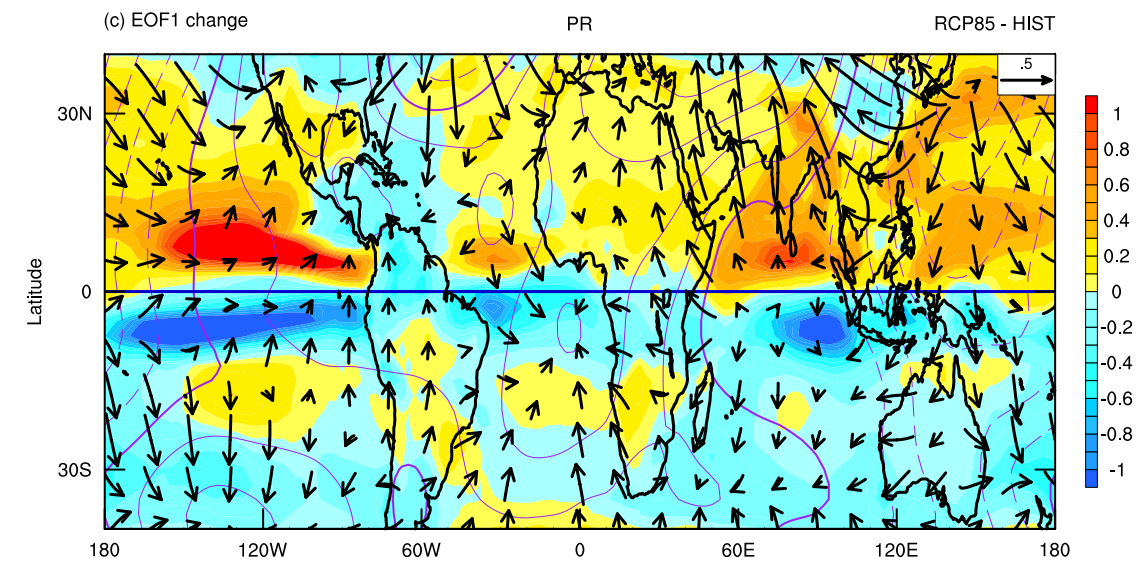
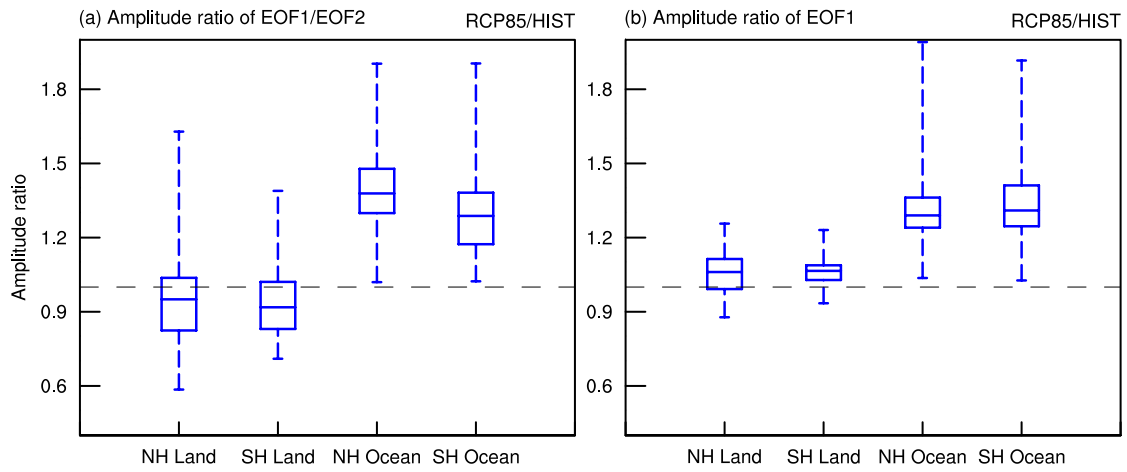
418 **Figure 1** The annual cycle of precipitation (unit: mm day⁻¹) in HIST runs (black line) and its future
 419 changes between RCP85 and HIST runs over (a) North Hemispheric (NH) land (0°-40°N), (b)
 420 South Hemispheric (SH) land (0°-40°S), (c) NH ocean (0°-40°N) and (d) SH land (0°-40°S). Box-
 421 plots for the future phase changes in the precipitation annual cycle over land and ocean from (e)
 422 CMIP5 monthly data and (f) CESM1 LENS daily data. The lines in each box represent the 25th
 423 percentile, median, and the 75th percentile, and the whiskers represent the minimum and maximum
 424 of the multi-model (or LENS) ensemble. In (f), the red and blue crosses indicate the phase changes
 425 between the 4xCO₂ and 1xCO₂ experiments of CESM1 with and without WES feedback,
 426 respectively.



427

428 **Figure 2** The spatial patterns of (a) EOF1 and (b) EOF2 in HIST runs and the corresponding
 429 normalized principle components (c) PC1 and (d) PC2 in HIST (black line) and their
 430 corresponding future changes between RCP85 and HIST. In a (b), overlaid as contours is the
 431 vertically-integrated MSE (unit: 10^7 J kg^{-1}) regressed upon the normalized PC1 (PC2) in HIST
 432 runs. The bold line indicates zero and solid (dashed) lines represent positive (negative) values with
 433 an interval of $0.5 \times 10^7 \text{ J kg}^{-1}$. Box-plots for (e) the phase changes and (f) the amplitude ratio
 434 between RCP85 and HIST for the two EOF modes from CMIP5 (blue) and CESM1 LENS (red).

435 The lines in each box represent the 25th percentile, median, and the 75th percentile, and the
436 whiskers represent the minimum and maximum of the multi-model (or LENS) ensemble.



438 **Figure 3** Box-plots comparing the ratio of the amplitude of (a) EOF1 over land $A_{1,L}$ divided by
439 EOF2 over land $A_{2,L}$ and EOF1 over ocean $A_{1,O}$ divided by EOF2 over ocean $A_{2,O}$ and (b) EOF1
440 over land $A_{1,L}$ and EOF1 over ocean $A_{1,O}$ between the RCP85 and HIST runs (i.e., RCP85 divided
441 by HIST) among CMIP5 models. Future change of (c) precipitation (shaded; unit: mm day^{-1}),
442 energy flux potential (contour; unit: W) and divergent energy flow (vectors; unit: 10^7 W m^{-1}) and
443 (d) TS (unit: K) regressed on the PC1 of precipitation annual cycle between the RCP85 and HIST
444 runs. In c, the bold line is zero and the solid (dashed) contours denote positive (negative) values
445 with the contour interval of $0.4 \times 10^{13} \text{ W}$. The line patterns over ocean in d have the same meaning
446 as c except that it is the change in the 1000 hPa wind speed congruent with EOF1 and the interval
447 is 0.2 m s^{-1} . The orange and blue contours over land in d indicate the 0.5 and -0.5 mm day^{-1} contours
448 of precipitation EOF1 shown in Fig. 2a, respectively, demarcating the boundaries of the land
449 monsoonal regions. The purple dots over land indicate regions of increased surface cooling
450 feedback parameter β under global warming. The horizontal lines in a and b represent the
451 minimum, 25th percentile, median, 75th percentile, and the whiskers are the maximum and
452 minimum values of the multi-model ensemble.

1 **Opposite phase changes of precipitation annual cycle over land and**
2 **ocean under global warming**

3 Fengfei Song¹, Jian Lu¹, L. Ruby Leung¹, Fukai Liu²

4 1. Atmospheric Sciences and Global Change Division, Pacific Northwest National Laboratory,
5 Richland, Washington, USA

6 2. Physical Oceanography Laboratory/CIMST, Ocean University of China and Qingdao National
7 Laboratory for Marine Science and Technology, Qingdao, China

8

9

10 **Supplementary information:**

11 One table and 6 Figures.

12

13 Submitted to *Geophysical Research Letters*

14

15

16

17

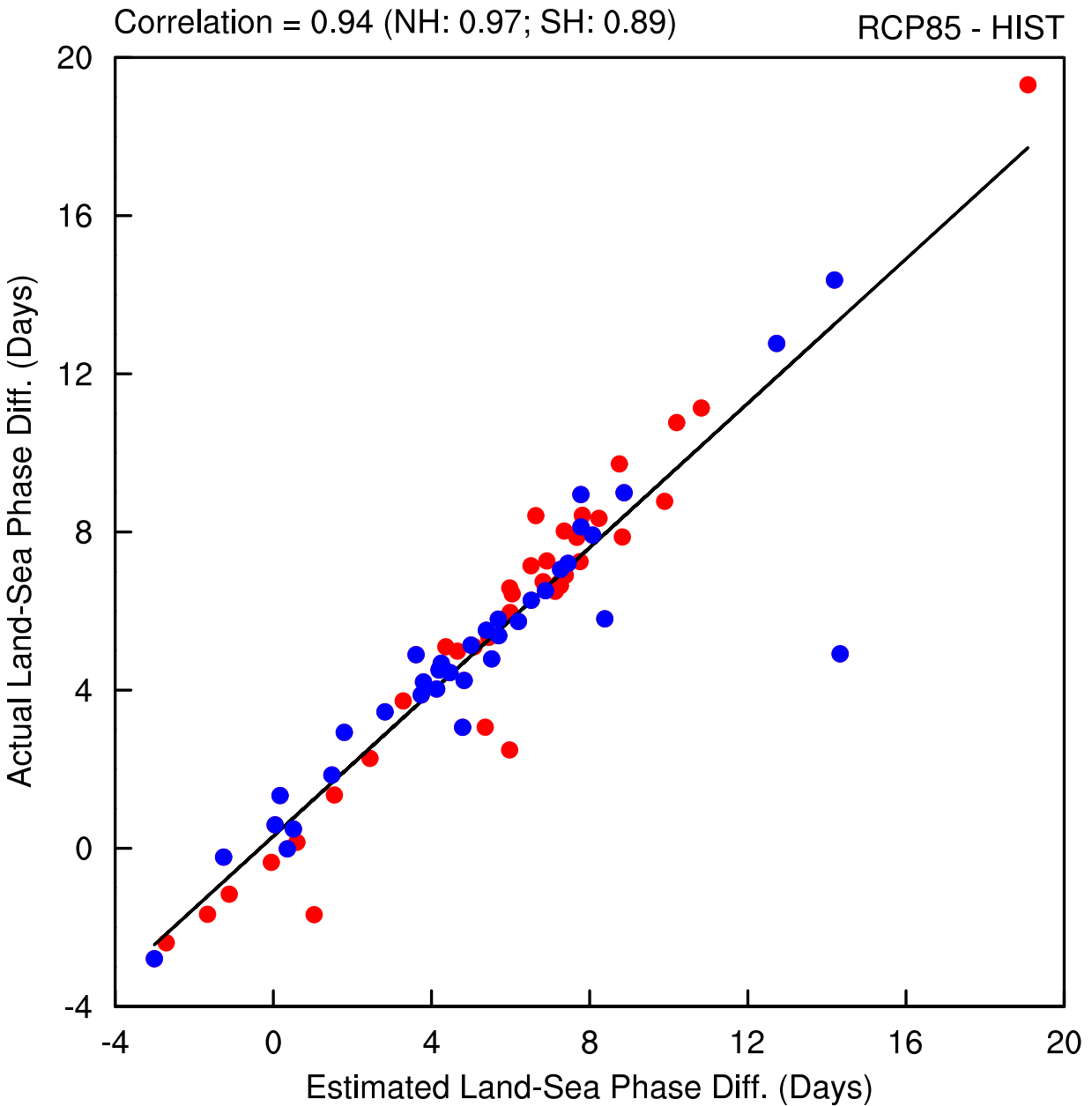
18 **Corresponding authors:**

19 Jian Lu (jian.lu@pnnl.gov) and L. Ruby Leung (ruby.leung@pnnl.gov)

20 **Supplementary Table 1** Data from the HIST and RCP85 simulations in 37 CMIP5 models used
 21 in this study.

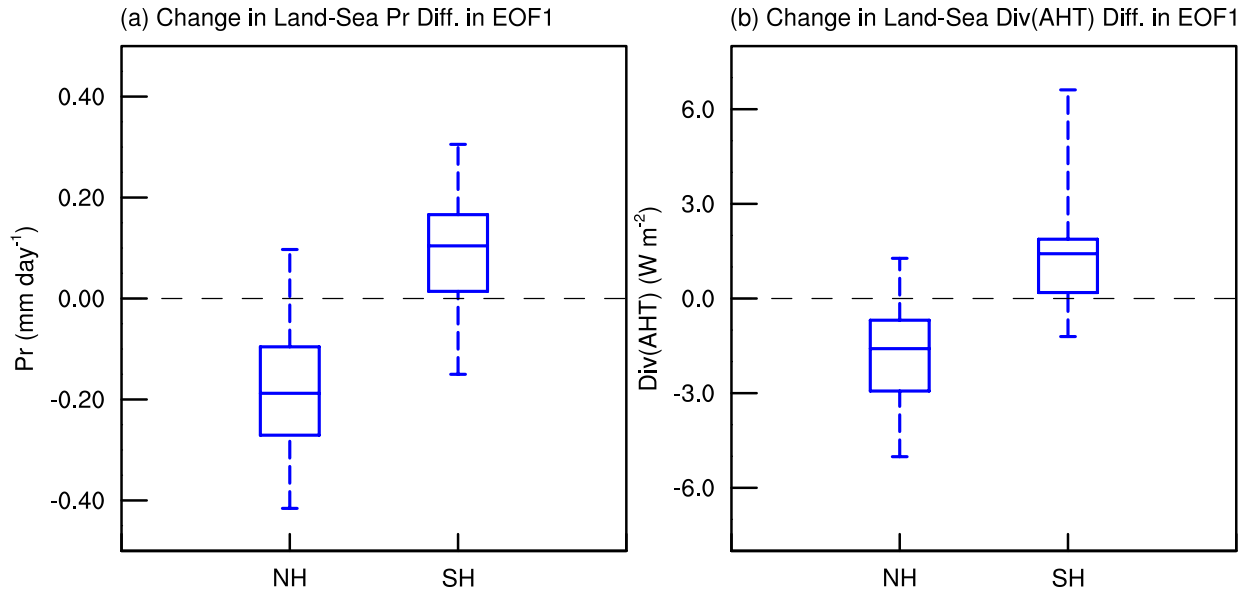
No.	Model	Energy fluxes	Other variables
1	ACCESS1-0	×	×
2	ACCESS1-3	×	×
3	bcc-csm1-1	×	×
4	bcc-csm1-1-m	×	×
5	BNU-ESM	×	×
6	CanESM2	×	×
7	CCSM4	×	×
8	CESM1-BGC	×	×
9	CESM1-CAM5	×	×
10	CESM1-WACCM	×	×
11	CMCC-CESM	×	×
12	CMCC-CM	×	×
13	CMCC-CMS	×	×
14	CNRM-CM5	×	×
15	CSIRO-Mk3-6-0	×	×
16	FGOALS-g2	×	×
17	FIO-ESM		×
18	GFDL-CM3	×	×
19	GFDL-ESM2G	×	×
20	GFDL-ESM2M	×	×
21	GISS-E2-H	×	×
22	GISS-E2-R	×	×
23	HadGEM2-AO		×
24	HadGEM2-CC	×	×
25	HadGEM2-ES	×	×
26	inmcm4	×	×
27	IPSL-CM5A-LR	×	×
28	IPSL-CM5A-MR	×	×
29	IPSL-CM5B-LR	×	×

30	MIROC5	×	×
31	MIROC-ESM-CHEM	×	×
32	MIROC-ESM	×	×
33	MPI-ESM-LR	×	×
34	MPI-ESM-MR	×	×
35	MRI-CGCM3	×	×
36	NorESM1-M	×	×
37	NorESM1-ME	×	×



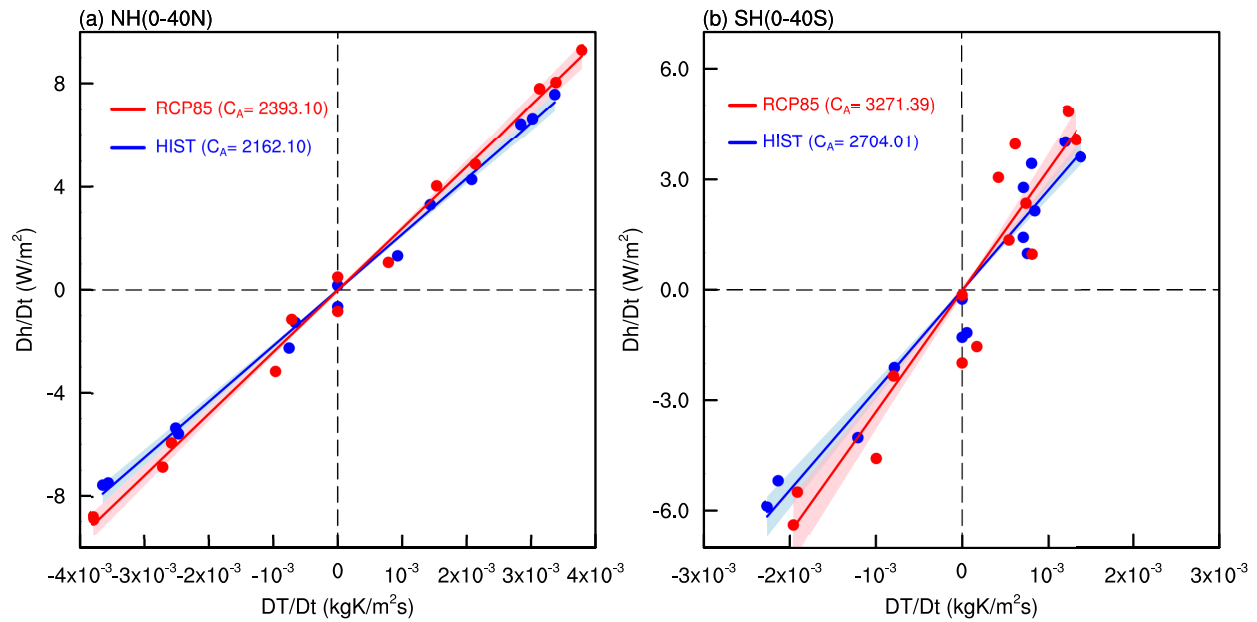
23

24 **Supplementary Fig. 1** Scatterplot between the change of the actual land-sea phase difference and
 25 the corresponding estimate (i.e., $\phi_L - \phi_O$) among the CMIP5 models in NH (red dots) and SH
 26 (blue dots). Each dot represents one model. Positive value indicates that land and ocean
 27 precipitation become more in phase with each other. The correlation is 0.97 in NH and 0.89 in SH,
 28 respectively.



29

30 **Supplementary Fig. 2** Box-plots for the change (RCP85 – HIST) in land-sea difference of (a)
 31 precipitation (unit: mm day⁻¹) and (b) divergence of atmospheric heat transport ($\nabla \cdot (AHT)$; unit:
 32 W m⁻²) regressed on the precipitation EOF1 among CMIP5 models.



33

34 **Supplementary Fig. 3** Scatterplot and regression between the monthly tendencies of $\langle h \rangle$ and $\langle T \rangle$.

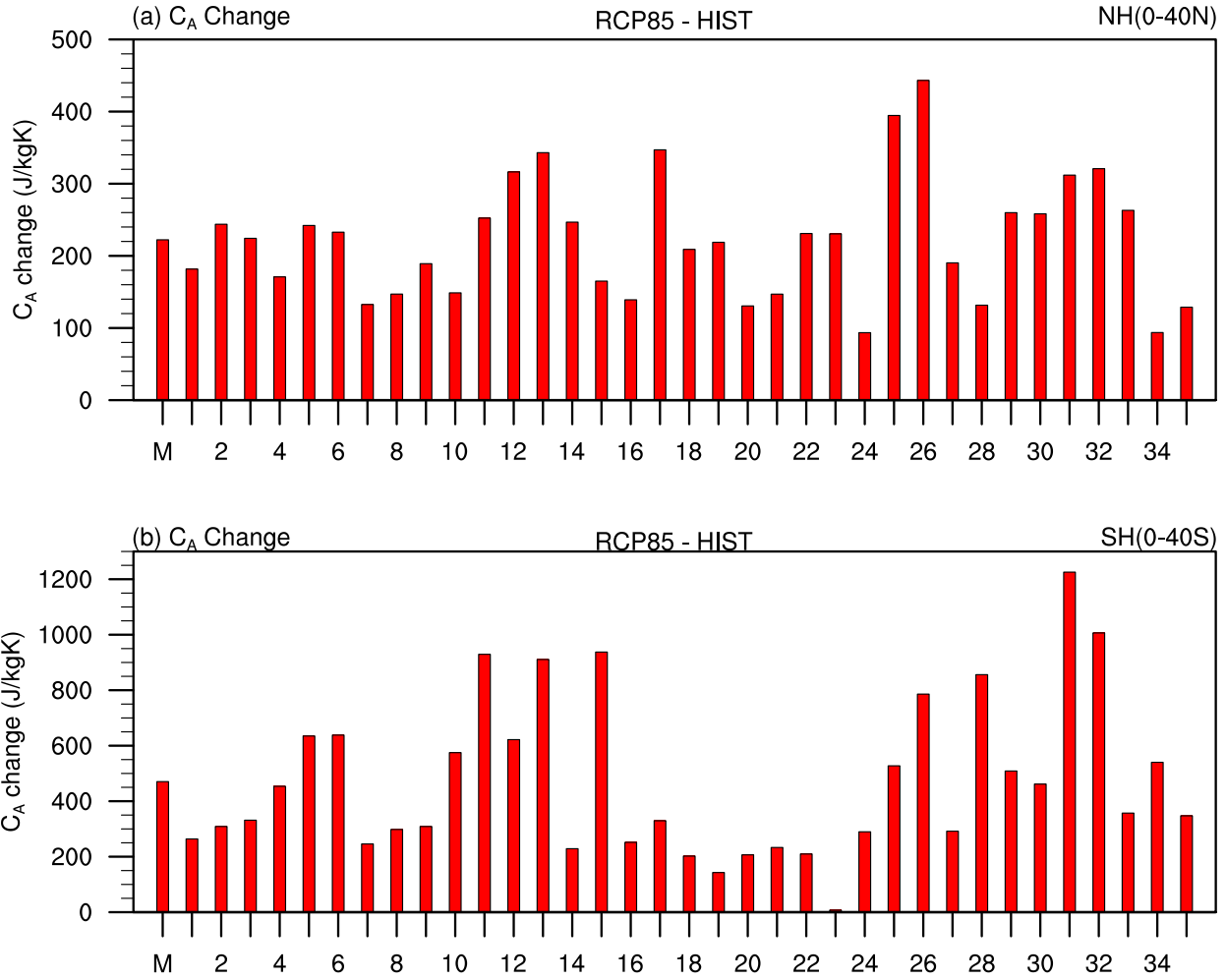
35 These tendencies are computed based on the multi-model ensemble mean climatological monthly

36 values averaged over (a) NH (0° - 40° N) and (b) SH (0° - 40° S), respectively. The regression slope

37 (C_A) provides an estimate of the effective atmospheric heat capacity in the hemisphere examined.

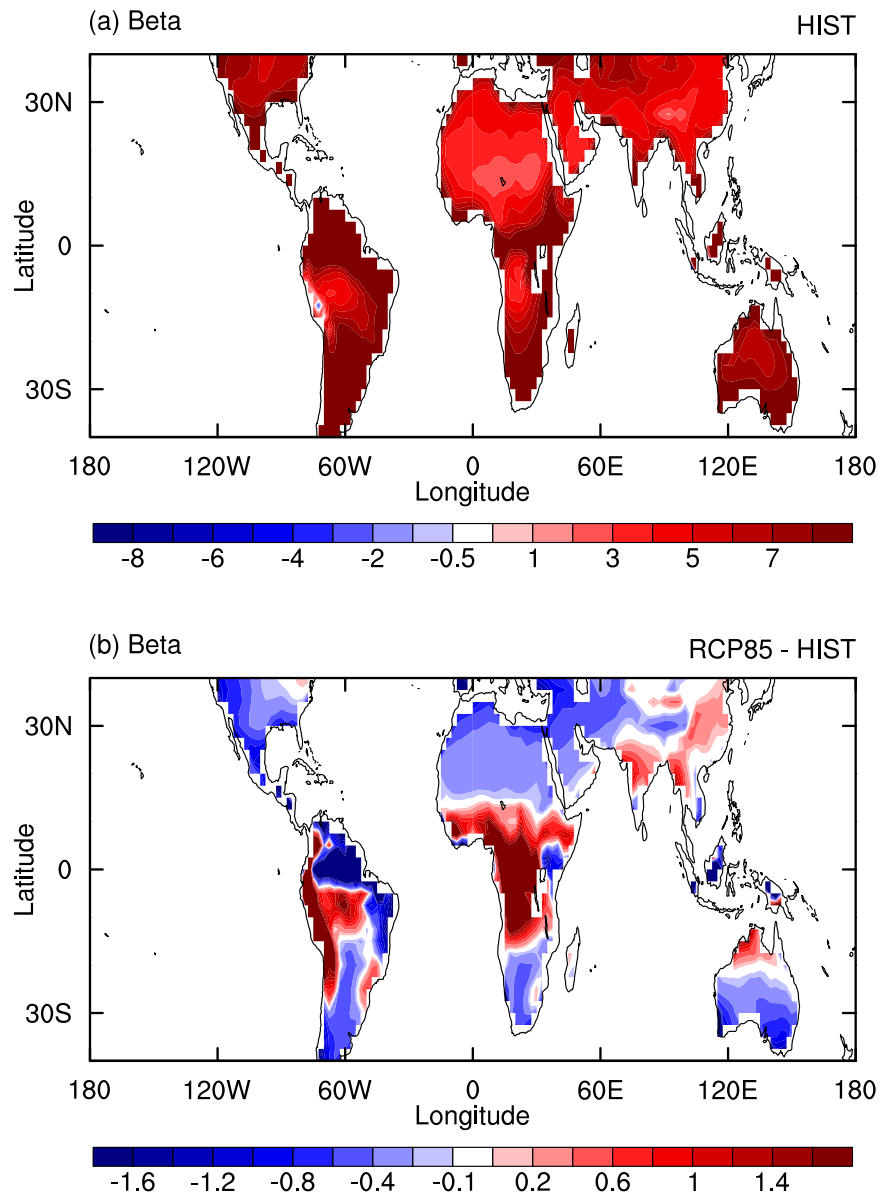
38 The blue and red dots and lines are for the HIST and RCP85 simulations, respectively. The shading

39 indicates one standard deviation of the regression slope among the CMIP5 models.



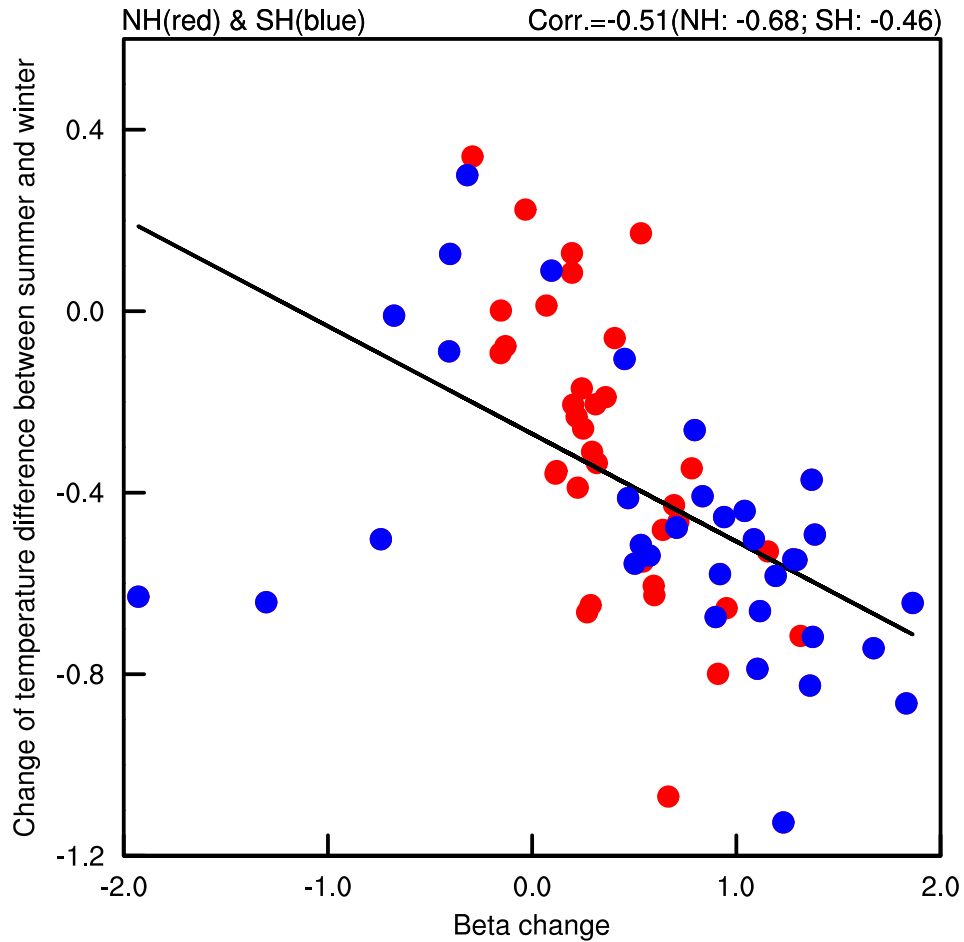
40

41 **Supplementary Fig. 4** The effective atmospheric heat capacity C_A changes between the RCP85
 42 and HIST experiments in the CMIP5 models in (a) NH (0° - 40° N) and (b) SH (0° - 40° S). M
 43 indicates the multi-model ensemble mean and each number denotes one of the 35 CMIP5 models.



44

45 **Supplementary Fig. 5** The surface cooling feedback parameter β in (a) the HIST run and (b) its
 46 change between the RCP85 and HIST runs.



47

48 **Supplementary Fig. 6** Scatterplot between the change of surface cooling feedback β and the
 49 temperature difference between summer (July-August-September (JAS) for NH and January-
 50 February-March (JFM) for SH) and winter (JFM for NH and JAS for SH) over the land monsoonal
 51 regions, which are defined as regions with the magnitude of precipitation anomalies in EOF1
 52 greater than 0.5 mm day^{-1} . Each dot represents one CMIP5 model with red (blue) for NH (SH).
 53 The correlations are listed at the upper-right corner of the figure, all being statistically significant
 54 at 1% level based on Student's t-test. Note that the correlation for SH can be augmented to -0.81
 55 when three outlier models (GFDL-ESM2G, GFDL-ESM2M and GISS-E2-H) are excluded.